

VIP **CO<sub>2</sub> Electroreduction** Very Important Paper
How to cite: *Angew. Chem. Int. Ed.* **2021**, *60*, 21952–21958

International Edition: doi.org/10.1002/anie.202108388

German Edition: doi.org/10.1002/ange.202108388

# Implanting Numerous Hydrogen-Bonding Networks in a Cu-Porphyrin-Based Nanosheet to Boost CH<sub>4</sub> Selectivity in Neutral-Media CO<sub>2</sub> Electroreduction

 Yi-Rong Wang<sup>+</sup>, Ming Liu<sup>+</sup>, Guang-Kuo Gao, Yi-Lu Yang, Ru-Xin Yang, Hui-Min Ding, Yifa Chen,<sup>\*</sup> Shun-Li Li, and Ya-Qian Lan<sup>\*</sup>

**Abstract:** The exploration of novel systems for the electrochemical CO<sub>2</sub> reduction reaction (CO<sub>2</sub>RR) for the production of hydrocarbons like CH<sub>4</sub> remains a giant challenge. Well-designed electrocatalysts with advantages like proton generation/transferring and intermediate-fixating for efficient CO<sub>2</sub>RR are much preferred yet largely unexplored. In this work, a kind of Cu-porphyrin-based large-scale ( $\approx 1.5 \mu\text{m}$ ) and ultrathin nanosheet ( $\approx 5 \text{ nm}$ ) has been successfully applied in electrochemical CO<sub>2</sub>RR. It exhibits a superior FE<sub>CH<sub>4</sub></sub> of 70 % with a high current density ( $-183.0 \text{ mA cm}^{-2}$ ) at  $-1.6 \text{ V}$  under rarely reported neutral conditions and maintains FE<sub>CH<sub>4</sub></sub> > 51 % over a wide potential range ( $-1.5$  to  $-1.7 \text{ V}$ ) in a flow cell. The high performance can be attributed to the construction of numerous hydrogen-bonding networks through the integration of diaminotriazine with Cu-porphyrin, which is beneficial for proton migration and intermediate stabilization, as supported by DFT calculations. This work paves a new way in exploring hydrogen-bonding-based materials as efficient CO<sub>2</sub>RR catalysts.

## Introduction

CO<sub>2</sub>, as a kind of notorious molecule and greenhouse gas, is thermodynamically stable and chemically inert due to the high bonding energy ( $750 \text{ kJ mol}^{-1}$ ) of C=O bond and catalysts are needed to activate and convert it into high-value added products.<sup>[1]</sup> Electrochemical CO<sub>2</sub> reduction reaction (CO<sub>2</sub>RR), is of vital importance for renewable energy storage and alleviating climate change since it allows for the

conversion of CO<sub>2</sub> into valuable chemicals or fuels by renewable electricity.<sup>[2]</sup> In particular, the highly selective production of hydrocarbon fuels (e.g., methane and ethylene) has received tremendous attention owing to their dominant positions in energy supply for both human life and industrial production.<sup>[3]</sup> Nevertheless, the major progress of electrochemical CO<sub>2</sub>RR has been generally limited to two-electron reduced products like CO or formate and the high-efficiency production of higher-value products involving multiple proton-coupled electron transfer (PCET) processes remains as one of the biggest scientific challenge.<sup>[4]</sup> Up to date, Cu-based catalysts have proven to be the most efficient in the production of hydrocarbons or alcohols owing to the negative adsorption energy for CO\* and positive adsorption energy for H\* compared with other transition-metal systems.<sup>[5]</sup> However, the state-of-the-art Cu-based CO<sub>2</sub>RR systems are still limited by several competing reactions such as surface oxidation or the thermodynamically favorable hydrogen evolution reaction (HER), in which each competitive reaction occurs via different intermediates and the unclear CO<sub>2</sub>RR mechanism concerning the tuning and stabilization of intermediates result in relatively low selectivity.<sup>[6]</sup> So, the design of Cu-based electrocatalysts has emerged to be the most challenging step in the development of tunable CO<sub>2</sub>RR systems for selective production of hydrocarbons or alcohols with high efficiency.

During the CO<sub>2</sub>RR process, the reaction intermediates play vital roles in the generation of high-value added products, which can determine the key or rate-determination steps.<sup>[7]</sup> Based on the molecular lengths, the reaction intermediates related to CO<sub>2</sub>RR can be classified into two groups: key intermediates with polyatomic length (e.g., \*COOH and \*OCHO, etc.) and competitive intermediates with monoatomic length (e.g., \*OH, \*CO and \*H, etc.).<sup>[8]</sup> The efficiency of CO<sub>2</sub>RR is well associated with the generation, binding and stabilization of these intermediates during the CO<sub>2</sub>RR process.<sup>[9]</sup> For example, in the pathway of CO<sub>2</sub> to CH<sub>4</sub>, the much favored process includes the binding of intermediate \*CO with H<sup>+</sup> to generate \*CHO, yet it is still restrained by the competitive \*CO desorption process to form CO and the sluggish eight-electron transfer process.<sup>[10]</sup> The efficient combination of intermediate \*CO with H<sup>+</sup> lies in the catalytic activity, H<sup>+</sup> migration and stabilization agents, in which high activity can ensure sufficient intermediates; H<sup>+</sup> migration or stabilization agents would enable the readily combination of \*CO with H<sup>+</sup> rather than desorption. To this end, the key steps are mostly restricted by the lack of desired platform that enable efficient generation, binding and most importantly,

[\*] Dr. Y.-R. Wang,<sup>[†]</sup> M. Liu,<sup>[†]</sup> G.-K. Gao, Y.-L. Yang, R.-X. Yang, H.-M. Ding, Prof. Y. Chen, S.-L. Li, Prof. Y.-Q. Lan  
Jiangsu Collaborative Innovation Centre of Biomedical Functional Materials, Jiangsu Key Laboratory of New Power Batteries  
School of Chemistry and Materials Science  
Nanjing Normal University  
Nanjing 210023 (P. R. China)  
E-mail: chyf927821@163.com  
yqlan@njnu.edu.cn

Prof. Y. Chen, Prof. Y.-Q. Lan  
School of Chemistry, South China Normal University  
Guangzhou, 510006 (P. R. China)  
E-mail: yqlan@m.scnu.edu.cn

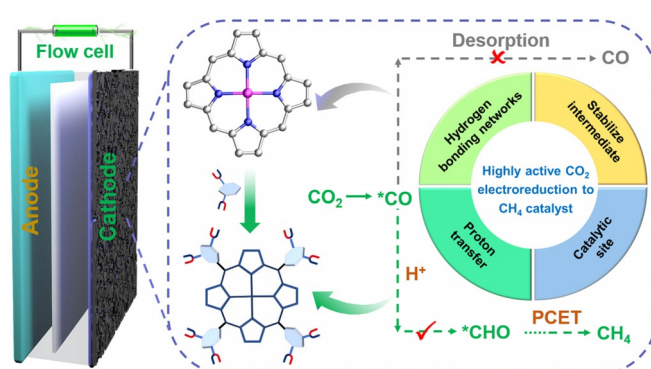
[†] These authors contributed equally to this work.

 Supporting information (including 41 figures and 4 tables) and the  ORCID identification number(s) for the author(s) of this article can be found under:  
<https://doi.org/10.1002/anie.202108388>.

stabilization of intermediates to facilitate the CO<sub>2</sub>RR process. Hydrogen bonding, a kind of flexible and highly reversible noncovalent bonds, has proven to be beneficial for the stabilization of specific intermediates and H<sup>+</sup> migration to change the pathway towards the formation of target products.<sup>[11]</sup> Nevertheless, there is few works about the control of PCET process for the CO\* to CH<sub>4</sub> production steps through hydrogen bonds, where it remains a grand difficulty to circumvent. In this regard, it is essential to explore powerful electrocatalysts with rich hydrogen bonding that might have positive effect on tuning the PCET processes for efficient production of hydrocarbon products like CH<sub>4</sub>.

With these considerations, hydrogen-bonded organic frameworks (HOFs) come to our mind as a prototype for designing efficient electrocatalysts. As a novel type of porous crystalline materials assembled by organic or metal-organic building blocks through hydrogen bonding interactions, HOFs possess unique features like easy recrystallization, regeneration and processing, holding much promise as efficient platform to stabilize the intermediates during the CO<sub>2</sub>RR process.<sup>[12]</sup> However, the applications of HOFs are generally limited by drawbacks like the structure fragility, originating from the weak nature of hydrogen bonds, oftentimes leading to the collapse of the frameworks after removal of solvent molecules. Over the past decades, a series of porous HOFs have been constructed through judicious selection of hydrogen-bonding motifs, which are further reinforced by other interactions such as  $\pi$ - $\pi$  stacking or van der Waals forces.<sup>[12a-c]</sup> By introducing special hydrogen-bonding motifs, robust and porous HOF structures with surface area as large as  $\approx 3500 \text{ cm}^2 \text{ g}^{-1}$  that are durable for the removal of solvent have been explored.<sup>[12a-c]</sup> The revelation that the much-improved stability of porous HOFs illuminates a distinct approach for designing novel HOF-based electrocatalysts. Specifically, the existence of tremendous hydrogen bonds in HOFs, if coupled with typical CO<sub>2</sub>RR centers like Cu-porphyrin and proton-generation units in suitable molecule distance, might make HOFs to be promising candidates in producing hydrocarbons like CH<sub>4</sub>.

As a proof-of-concept, we intend to choose copper porphyrin-based building block decorated with diaminotriazine moiety to construct HOFs so as to verify the feasibility of this inference. The relative considerations are listed as follows: 1) diaminotriazine moiety, a well-known synthon for constructing hydrogen bonding, would construct numerous hydrogen bonding networks and serve as “proton pump” to transfer protons when triggered by electricity stimulus;<sup>[13]</sup> 2) copper porphyrin has proven to be beneficial for the hydrocarbon production in CO<sub>2</sub>RR;<sup>[7a,14]</sup> 3) if the distance of diaminotriazine group and copper porphyrin is suitable, where sufficient H<sup>+</sup> can be transferred effectively to copper porphyrin center to largely promote the PCET process of CO<sub>2</sub>RR and 4) the integrated system with tremendous hydrogen bonding in the structure might be much beneficial for the specific intermediate-stabilization and H<sup>+</sup> migration to change the CO<sub>2</sub>RR pathway towards target products (Scheme 1). From the above we deduce that HOFs with such design principle will probably be promising candidates to



**Scheme 1.** Illustration of the advantages of Cu-TDPP-NS in electrochemical CO<sub>2</sub>RR.

enhance the efficiency and selectivity of hydrocarbons in CO<sub>2</sub>RR.

Herein, we have synthesized a kind of hydrogen-bonding organic framework assembled from diaminotriazine moiety decorated copper porphyrin units and successfully exfoliated it into large-scale ( $\approx 1.5 \mu\text{m}$ ) and ultrathin ( $\approx 5 \text{ nm}$ ) nanosheet (NS) to investigate the CO<sub>2</sub>RR performance. The combination of diaminotriazine and copper porphyrin in Cu-TDPP-NS can serve as the role of “proton pump” and active center in electrocatalytic CO<sub>2</sub>RR (Scheme 1). Specifically, Cu-TDPP-NS exhibits a superior FE<sub>CH<sub>4</sub></sub> of 70% with large current-density ( $-183.0 \text{ mA cm}^{-2}$ ) at  $-1.6 \text{ V}$  under neutral condition and keeps higher than 51% over a wide potential range ( $-1.5$  to  $-1.7 \text{ V}$ ). The electrochemical CO<sub>2</sub>RR under neutral condition has been rarely reported and the achieved performance is even superior to most of CO<sub>2</sub>RR systems under alkaline condition as far as we known. Based on experimental results and density functional theory (DFT) calculations, we illustrate the possible CO<sub>2</sub>RR mechanism, in which diaminotriazine group serving as the “proton pump” can construct hydrogen-bonding networks; the generated numerous hydrogen bonding networks in the structure can stabilize the intermediates and efficiently transfer the proton to copper porphyrin, resulting in the efficient combination of H<sup>+</sup> and \*CO to produce CH<sub>4</sub>. This work paves a new way in exploring novel hydrogen-bonding based electrocatalysts in efficient electrochemical CO<sub>2</sub>RR.

## Results and Discussion

For the preparation of Cu-TDPP and its nanosheet, Cu-TDPP is firstly prepared and characterized. Cu-TDPP, possessing a structure isomorphic to HOF-7, is synthesized via a facile solvothermal method. Cu-TDPP belongs to the triclinic system with space group of  $P\bar{1}$ .<sup>[15]</sup> It presents a 3D layer network, in which subunit of TDPP is connected by the intermolecular hydrogen-bonding and  $\pi$ - $\pi$  interaction, displaying a microporous structure with two kinds of pore-sizes (i.e.  $3.2 \times 4.7 \text{ \AA}^2$  and  $4.2 \times 6.7 \text{ \AA}^2$ ) (Figures 1b and S1). The powder X-ray diffraction (PXRD) pattern confirms that the as-synthesized Cu-TDPP is well crystalline, which is similar to simulated pattern (Figure 1a). The chemical component of

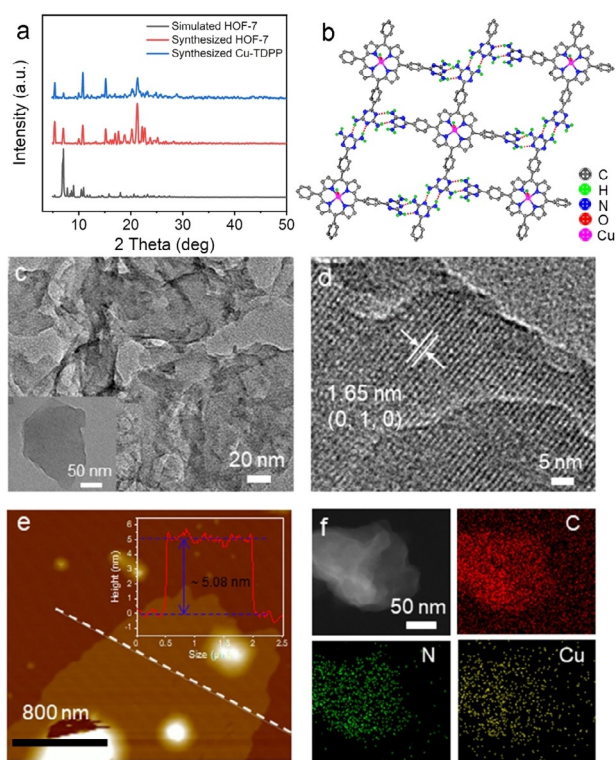


**Figure 1.** Structure and characterization of Cu-TDPP and Cu-TDPP-NS. a) PXRD pattern of Cu-TDPP. b) Hydrogen-bonding interactions in Cu-TDPP. c) TEM image of Cu-TDPP-NS. d) HRTEM image of Cu-TDPP-NS. e) AFM image and height profile of Cu-TDPP-NS. f) STEM and elemental mapping images of Cu-TDPP-NS.

Cu-TDPP is verified by Fourier transform infrared spectra (Figure S2). The N-H in-plane vibration at  $964\text{ cm}^{-1}$  is significantly changed and a new absorption peak appeared at  $999\text{ cm}^{-1}$  when compared with TDPP, indicating that the hydrogen proton is substituted by copper ion.<sup>[16]</sup> The disappearance of N-H stretching vibration at  $3315\text{ cm}^{-1}$  further confirms that the metal coordination occurred at the porphyrin center (Figure S2). To evaluate the  $\text{CO}_2$  sorption ability of Cu-TDPP, the  $\text{CO}_2$  sorption test is carried out and Cu-TDPP presents  $\text{CO}_2$  uptake capacity of  $10.1\text{ cm}^3\text{ g}^{-1}$  and  $6.5\text{ cm}^3\text{ g}^{-1}$  at  $273\text{ K}$  and  $298\text{ K}$ , respectively (Figure S3). The porosity of Cu-TDPP is further certified by the thermogravimetric analysis tests conducted under  $\text{N}_2$  atmosphere with a heating rate of  $10^\circ\text{C min}^{-1}$ . The result shows that Cu-TDPP loses the guest molecules in the temperature range from  $25$  to  $\approx 250^\circ\text{C}$ , resulting in the desolvated framework (Figure S4). Furthermore, Cu-TDPP can maintain crystalline structure in aqueous PBS solution ( $\approx 0.5\text{ M}$ ,  $\text{pH } 7$ ) for more than 12 h as proved by the PXRD tests, probably attributed to the robust 3D  $\pi$ - $\pi$  stacking structure and would guarantee the further investigation of  $\text{CO}_2\text{RR}$  (Figure S5).

In the structure of Cu-TDPP, two types of hydrogen bonding interactions involving the diaminotriazine motifs are discovered, namely, the type I in head-to-head mode and type II in head-to-waist mode (Figure 1b).<sup>[12a-c]</sup> Through these hydrogen-bonding interactions, Cu-TDPP molecules are self-assembled into a two-dimensional (2D) supramolecular layer.

By virtue of the hydrogen-bonding interaction between the coordinated water and the diaminotriazine segment, the two neighboring layers are connected together and further packed into a 3D framework via the intermolecular  $\pi$ - $\pi$  interaction between Cu-TDPP molecules (Figure S1). Owing to its unique layer-arrangement configuration with  $\pi$ - $\pi$  stacking interactions, Cu-TDPP itself tends to exhibit bulk and layer aggregated morphology, which is also proved by the scanning electron microscopy (SEM) and transmission electron microscopy (TEM) tests (Figure S6). To understand the interaction of intralaminar and layer hydrogen bonding, DFT calculations are performed to calculate the interaction energy. The results show that the layer interaction energy ( $-10.7\text{ kcal mol}^{-1}$ ) is lower than the intralaminar interaction energy ( $-13.37\text{ kcal mol}^{-1}$ ). Therefore, the 3D framework of Cu-TDPP assembled from 2D supramolecular layer has much potential in exfoliation treatment to transfer the bulk morphology into nanosheet and simultaneously expose more catalyst sites, which might be more beneficial for high-performance  $\text{CO}_2\text{RR}$ .

As a proof-of-concept, we set out to explore the exfoliation of Cu-TDPP. After high-frequency sonication for 30 min, the original bulk crystals ( $> 1\text{ }\mu\text{m}$ ) can be readily transformed into nanosheet (NS) as proved by the TEM test (Figure 1c). To evaluate the thickness of the obtained Cu-TDPP-NS, atomic force microscope (AFM) tests have been conducted. The results show that the thickness of Cu-TDPP-NS is  $\approx 5.08\text{ nm}$  over a large scale ( $\approx 1.5\text{ }\mu\text{m}$ ), which may be ascribed to the relatively weak interaction between the layers that is easy to break during the stripping process (Figure 1e). Furthermore, oriented lattice fringes can be observed in high-resolution TEM (HR-TEM) images and the lattice spacing of  $1.65\text{ nm}$  is assigned to the (010) plane of Cu-TDPP, confirming the high crystallinity of the obtained Cu-TDPP-NS (Figure 1d). Moreover, the scanning transmission electron microscopy (STEM) image and the corresponding energy dispersive X-ray element mapping of Cu-TDPP-NS show that C, N, O and Cu elements are uniformly distributed in the nanosheet, suggesting the high elemental homogeneity in the nanosheet (Figure 1f). The Cu content in Cu-TDPP-NS is determined to be  $\approx 4.8\text{ wt } \%$  by EDS test, which matches well with the result in inductively coupled plasma optical emission spectrometry ( $\approx 4.82\text{ wt } \%$ ) (Figure S7). The above results suggest that Cu-TDPP-NS with ultrathin thickness can be readily produced through a facile high-frequency sonication process and the specially designed structure might serve as the desirable platform to investigate the generation of high-value added products in  $\text{CO}_2\text{RR}$ .

The electrochemical  $\text{CO}_2\text{RR}$  performance of the catalyst is evaluated in flow cell ( $\approx 0.5\text{ M}$  PBS ( $\text{pH } 7$ ) as electrolyte) at selected potentials to determine the  $\text{CO}_2\text{RR}$  selectivity. According to the linear sweep voltammetry (LSV) curves, Cu-TDPP-NS presents a total current density of  $-310.2\text{ mA cm}^{-2}$  at  $-1.7\text{ V}$ , which is superior to Cu-TDPP ( $-222.8\text{ mA cm}^{-2}$ ) (Figure 2a). Besides, Cu-TDPP-NS has much larger current density in  $\text{CO}_2\text{RR}$  than that in HER, indicating Cu-TDPP-NS strongly favors  $\text{CO}_2\text{RR}$  than HER (Figure S12a). To evaluate the selectivity of samples for  $\text{CO}_2\text{RR}$ , the electrolysis is performed, and the gas/liquid products are monitored by gas

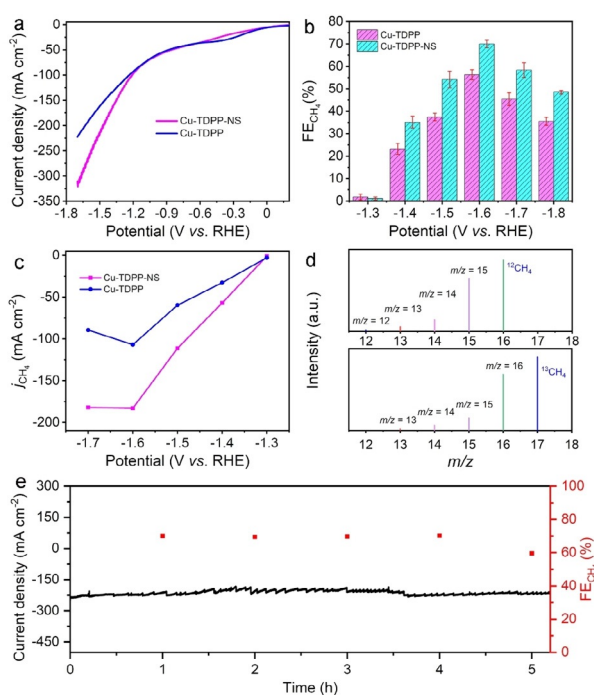


**Figure 2.** Electrocatalytic performance of Cu-TDPP and Cu-TDPP-NS. a) LSV curves. b) FE for CH<sub>4</sub> at different applied potentials. c) Partial CH<sub>4</sub> current density. d) Mass spectra of <sup>12</sup>CH<sub>4</sub> and <sup>13</sup>CH<sub>4</sub> recorded under <sup>12</sup>CO<sub>2</sub> and <sup>13</sup>CO<sub>2</sub> atmosphere, respectively. e) Durability test of Cu-TDPP-NS at the potential of −1.6 V vs. RHE.

chromatography and <sup>1</sup>H nuclear magnetic resonance spectroscopy, respectively (Figures S8–S11). As a result, the CH<sub>4</sub> is found to be the dominant product and there is no liquid product (Figures S8–S11). For Cu-TDPP-NS, it gives the highest FE<sub>CO</sub> (75.5%) at −1.3 V with a current density of −129.7 mA cm<sup>−2</sup> along with 16.1% FE<sub>H<sub>2</sub></sub> and negligible CH<sub>4</sub> (0.9%) or C<sub>2</sub>H<sub>4</sub> (2.8%). With the increase of potential, the FE<sub>CH<sub>4</sub></sub> continuously increases and reaches up to 70% at −1.6 V and keeps higher than 51% over a wide potential range from −1.5 to −1.7 V in PBS solution (pH 7) (Figure 2b). The highest FE<sub>CO<sub>2</sub>RR</sub> is 83.4% at −1.6 V and keeps higher than 72% from −1.3 to −1.6 V (Figure S13). The reported electrochemical CO<sub>2</sub>RR systems are generally conducted with alkaline electrolytes and works are limited to less than a handful of systems that are performed under approximate neutral conditions.<sup>[5b,6b,8a]</sup> This is one of the pioneering systems to achieve CO<sub>2</sub>RR to CH<sub>4</sub> with high selectivity under neutral condition and the achieved performance is even superior to most of CO<sub>2</sub>RR systems under alkaline condition (Table S1).<sup>[3b,11a,14,17]</sup> In contrast, Cu-TDPP gives a large FE<sub>H<sub>2</sub></sub> (55.7%) at −1.3 V with a current density of −114.2 mA cm<sup>−2</sup> and the highest FE<sub>CH<sub>4</sub></sub> is only 55.9% at −1.6 V (Figures 2b and S14a, c). The superior performance of Cu-TDPP-NS indicates the advantage of nanosheet morphology in CO<sub>2</sub>RR.

To further reveal the activity of Cu-TDPP-NS, partial current densities of CH<sub>4</sub>, CO, C<sub>2</sub>H<sub>4</sub> and H<sub>2</sub> at different potentials are calculated (Figure 2c and Figure S12d). Cu-TDPP-NS displays a partial CH<sub>4</sub> current density of −183.0 mA cm<sup>−2</sup> at −1.6 V, which is almost twice than that

of Cu-TDPP (−107.0 mA cm<sup>−2</sup>) (Figure 2c). Besides, to reveal the carbon source of CO<sub>2</sub>RR products, an isotopic experiment that using <sup>13</sup>CO<sub>2</sub> as substrate is performed under identical reaction condition. The products are analyzed by gas chromatography and mass spectra. As shown in Figure 2d and Figure S15, the peaks at *m/z* = 17, 29 and 30 are assigned to <sup>13</sup>CH<sub>4</sub>, <sup>13</sup>CO and <sup>13</sup>C<sub>2</sub>H<sub>4</sub>, respectively, indicating the carbon sources of CH<sub>4</sub>, CO and C<sub>2</sub>H<sub>4</sub> indeed derive from the CO<sub>2</sub> used. Besides, the bare carbon paper and carbon paper decorated with Nafion are measured as comparisons and no electrocatalytic CO<sub>2</sub>RR activity are detected (Figures S16 and S17). Moreover, sufficient control experiments have been performed to support the vital role of catalyst (Figures S18–S20). Firstly, PTFE and PVDF are used as binders to fabricate the working electrodes. The results show that the Cu-TDPP-NS can reach up to the highest FE<sub>CH<sub>4</sub></sub> = 68% and 70% at −1.6 V when PTFE and PVDF are applied, respectively (Figure S18 and S19). The remained high FE<sub>CH<sub>4</sub></sub> indicate the binder has no apparent effect on the generation of electrocatalytic products. Besides, carbon cloth is applied to replace carbon paper. The results show that the FE<sub>CH<sub>4</sub></sub> of Cu-TDPP-NS can reach up to 71% at −1.6 V, which is close to the result that applying carbon paper (Figure S20). When dispersing the Cu-TDPP-NS on KB carbon, it can be found that the increase of current density at each potential compared with the bare one, the achieved highest FE<sub>CH<sub>4</sub></sub> centers at potential from −1.6 V to −1.5 V yet the relative FE<sub>CH<sub>4</sub></sub> value decreases from 70% to 55% (Figure S21). In addition, to further evaluate the selectivity of Cu-TDPP-NS for CO<sub>2</sub>RR under low CO<sub>2</sub> concentration, 30% concentration of CO<sub>2</sub> is applied as the gas source and tested under identical reaction condition. The maximum FE<sub>CH<sub>4</sub></sub> of Cu-TDPP-NS can reach up to 37.5% at −1.6 V, indicating Cu-TDPP-NS can maintain its activity under low CO<sub>2</sub> concentration (Figure S22).

To study the electrocatalytic kinetics on the electrode/electrolyte surface during CO<sub>2</sub>RR, electrochemical impedance spectroscopy tests of the samples are performed (Figure S23). As revealed by the Nyquist plots, Cu-TDPP-NS has much smaller charge transfer resistance (19.83 Ω) than that of Cu-TDPP (23.98 Ω), confirming faster electron transfer efficiency for Cu-TDPP-NS.

Stability is a crucial criterion to evaluate the durability properties of catalysts for further applications. To analyze the electrochemical stability of Cu-TDPP-NS, longtime durability test is assessed with chronoamperometric curves at −1.6 V (Figure 2e). After 5 h, the FE<sub>CH<sub>4</sub></sub> of Cu-TDPP-NS can be maintained higher than 60% and the current density remains at about −216 mA cm<sup>−2</sup>. For ICP-MS results, the Cu detected in the test is below the detection limit (Table S2). These results demonstrate that Cu-TDPP-NS is a kind of stable electrocatalyst, which has much potential to be used in efficient CO<sub>2</sub>RR (Figures S24–S26). To further investigate the structural stability of these electrocatalysts during the CO<sub>2</sub>RR process, XAS is performed. The results show that no significant change in Cu K-edges and no visible metallic Cu<sup>0</sup> signals could be observed in the X-ray absorption near-edge structure (XANES) profiles of Cu-TDPP-NS after electrocatalytic process (Figure 3a), and no obvious signal of Cu-Cu

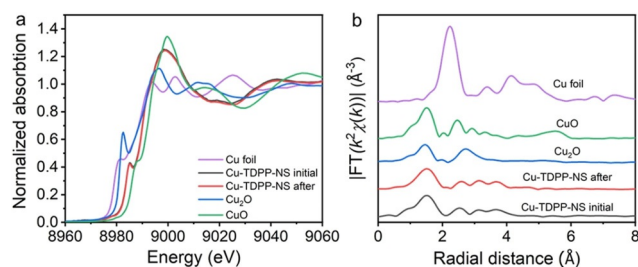


**Figure 3.** XAS measurements. a) Cu K-edge XANES spectra of Cu foil,  $\text{Cu}_2\text{O}$ , CuO, and Cu-TDPP-NS samples before and after  $\text{CO}_2\text{RR}$ . b) Cu K-edge FT spectra of Cu foil,  $\text{Cu}_2\text{O}$ , CuO, and Cu-TDPP-NS before and after  $\text{CO}_2\text{RR}$ .

bond is observed in the extended X-ray absorption fine structure (EXAFS) spectrum (Figure 3b).<sup>[18]</sup>

To reveal the superiority of Cu-TDPP-NS, contrast samples including 5,10,15,20-tetrakis(*para*-aminophenyl)-21*H*,23*H*-porphyrin copper (Cu-TAPP), 5,10,15,20-tetrakisphenyl-porphyrin copper (Cu-TPP), and melamine are prepared and measured (Figure 4a and Figures S27–S31). Cu-TAPP and Cu-TPP are similar to Cu-TDPP, in which the diaminotriazine moieties is replaced by amino groups for Cu-TAPP and Cu-TPP is the one without the diaminotriazine moieties. Melamine is to stimulate the diaminotriazine moiety and investigate its  $\text{CO}_2\text{RR}$  performance. The current density of Cu-TDPP-NS ( $-310.2 \text{ mA cm}^{-2}$ ) is higher than those of Cu-TAPP ( $-185.6 \text{ mA cm}^{-2}$ ), Cu-TPP ( $-240.8 \text{ mA cm}^{-2}$ ) and melamine ( $-128.0 \text{ mA cm}^{-2}$ ) at  $-1.7 \text{ V}$  (Figure 4b). Cu-TAPP exhibits a maximum  $\text{FE}_{\text{CH}_4}$  of 25.9% at  $-1.5 \text{ V}$ , which

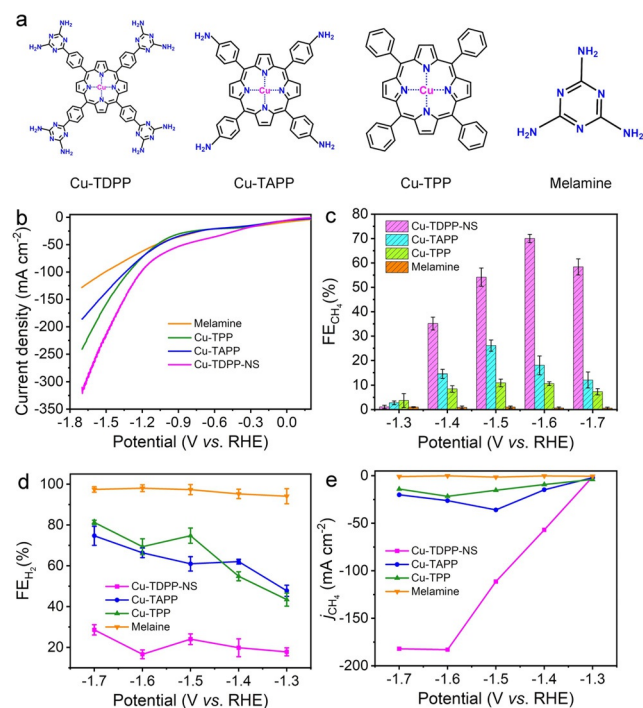


**Figure 4.** Electrocatalytic performance of Cu-TDPP-NS, Cu-TAPP, Cu-TPP and melamine. a) Molecular structures. b) LSV curves. c) FE for  $\text{CH}_4$  at different applied potentials. d) FE for  $\text{H}_2$  at different applied potentials. e) Partial  $\text{CH}_4$  current density.

is much lower than that of Cu-TDPP-NS (70%,  $-1.6 \text{ V}$ ) (Figures 4c and S32). Similar result is also detected for Cu-TPP, in which the  $\text{FE}_{\text{CH}_4}$  is only 10.8% at  $-1.6 \text{ V}$  (Figures 4c and S33). Melamine presents negligible  $\text{CO}_2$  reduction activity (Figures 4c and S34) and TDPP has no  $\text{CO}_2\text{RR}$  activity (Figure S35). Besides, the partial current densities of  $\text{CH}_4$  for Cu-TAPP, Cu-TPP and melamine are calculated  $-26.2$ ,  $-21.7$  and  $-0.11 \text{ mA cm}^{-2}$  at  $-1.6 \text{ V}$ , respectively, which is much lower than that of Cu-TDPP-NS (Figure 4e). In addition, the charge transfer resistance of Cu-TDPP-NS, Cu-TAPP, Cu-TPP and melamine are calculated to be 19.83, 33.83, 42.58 and  $84.05 \Omega$ , respectively, demonstrating faster electron transfer efficiency for Cu-TDPP-NS (Figure S36). Moreover, the KIE measurements of Cu-TDPP-NS, Cu-TAPP, Cu-TPP and melamine are performed to provide information regarding the rate-determining step in the proposed  $\text{CO}_2\text{RR}$  mechanism.<sup>[19]</sup> Cu-TDPP-NS shows a KIE = 1.89, which is larger than Cu-TAPP (1.18), Cu-TPP (1.18) and melamine (1.05), suggesting a rate-determining proton transfer step in the mechanism. The KIE value of Cu-TDPP-NS can serve as another vital evidence to support the DFT calculation results.

To understand the high activity as well as the selective reaction mechanism of Cu-TDPP-NS, DFT based computational approaches are implemented (Figure S37). Abstractly, diaminotriazine is found to play two roles in improving the activities and selectivity, which are (i) the “proton pump” that can improve the proton donation efficiency, and (ii) the “intermediate fixator” that helps to make intermediates (e.g.,  $^*\text{COOH}$ ) more favorable to adsorb and stabilize. The next two paragraphs will demonstrate them more specifically.

We started from the protonation efficiency for  $\text{CO}_2\text{RR}$  and HER on Cu-TDPP-NS and Cu-TPP, by investigating and comparing the reaction barriers of their first steps (proton coupled  $\text{CO}_2$  and  $\text{H}^+$  adsorption, RS3 and RS1) that is essential to the selectivity (Figures 5a, b and S38, Movies 1–4). From the calculated free energy diagrams, the protonation barriers for  $\text{CO}_2\text{RR}$  and HER on Cu-TPP are the formation of adsorbed intermediates  $^*\text{COOH}$  and  $^*\text{H}$  with rather high free energies of 0.97 and 2.49 eV, respectively (Figure 5a). Instead, Cu-TDPP-NS, in which the diaminotriazine is applied to replace benzene moiety in Cu-TPP, possesses remarkably reduced barriers (0.51 and 1.35 eV) (Figure 5a). These results indicate that Cu-TDPP-NS and Cu-TPP both strongly favor the  $\text{CO}_2\text{RR}$  over HER, and the  $\text{CO}_2\text{RR}$  and HER are sluggish in Cu-TPP than Cu-TDPP-NS. More intrinsically, the reason for such improved proton donation efficiency in Cu-TDPP-NS can be attributed to an extra stabilization effect to  $\text{OH}^-$  via an extra hydrogen-bonding provided by the amino group of diaminotriazine in Cu-TDPP-NS, as seen from the fifth panel in Figure 5b. This is similar to the famous strategy to improve the proton donation efficiency of  $\text{H}_2\text{O}$  by using catalyst that bond strongly to  $\text{OH}^*$  in water splitting.<sup>[20]</sup> These results indicate that the first “proton pump” role of diaminotriazine that improves the proton donation efficiency as proved by KIE measurements.

The second role is unfolded via the calculations of reaction free energy diagram (FED) for  $\text{CO}_2\text{RR}$  and HER, as shown in Figures 5c, d, S39, and S40. As for formic acid

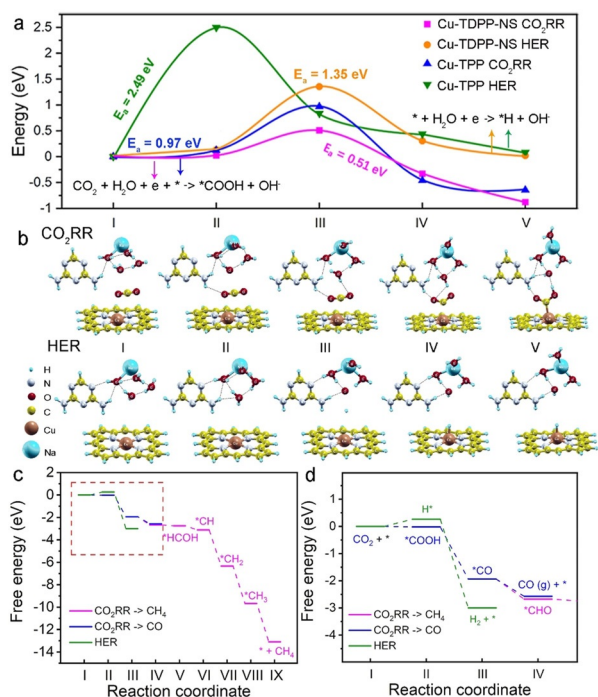


**Figure 5.** DFT calculations and the proposed reaction mechanism. a) Free energy diagrams of CO<sub>2</sub>RR and HER for Cu-TDPP-NS and Cu-TTP. b) Reactions snapshots of CO<sub>2</sub>RR and HER on Cu-TDPP-NS at different reaction coordinates. c, d) Free energy diagrams of CO<sub>2</sub> reduction to CH<sub>4</sub> (pink) and CO (blue), and HER (green) for Cu-TDPP-NS. (d) is an enlargement of the section marked in (c).

pathway, the formation free energy of \*OCHO are 2.20 and 2.31 eV at  $-1.5$  V for Cu-TDPP-NS and Cu-TTP, respectively. These values are far higher than that of COOH\* (Figure S40), indicating the unfavourability of formic pathway on both of catalysts. This result is further supported by the <sup>1</sup>H NMR result that no HCOOH has been detected in the electrocatalytic products (Figure S11). From the calculated free energy diagrams, the formation of \*COOH has a  $-0.28$  eV free energy compared to \*H on Cu-TDPP-NS, which is much lower than Cu-TTP ( $\Delta G = -0.12$  eV). This result is consistent with the higher CO<sub>2</sub>RR activity and selectivity of Cu-TDPP-NS than Cu-TTP, complying with the kinetic results as mentioned above. These results may be attributed to the vital role of hydrogen-bonding in Cu-TDPP-NS that can stabilize the \*COOH. This reveals the second role of diaminotriazine that is more favorable to absorb and stabilize COOH\* over H<sup>+</sup>, i.e., the “intermediate fixator”, which improves the CO<sub>2</sub>RR selectivity.

Moreover, from Figure 5c,d, we can understand the potential dependent FE of CO and CH<sub>4</sub>. For the possible generation of \*CHO or CO in the next step, \*CHO ( $\Delta G = -0.74$  eV) is more thermodynamic favorable than CO ( $\Delta G = -0.64$  eV). This result is further supported by the relative lower selectivity for the CO at low potential (Figure S12). The following pathways like the stepwise reduction of \*CHO into \*HCOH, \*CH, \*CH<sub>2</sub>, \*CH<sub>3</sub> and finally CH<sub>4</sub> are thermodynamically feasible. In a word, the sequence of reaction energies is well consistent with the higher CH<sub>4</sub> selectivity of diaminotriazine modified Cu-TDPP-NS over contrast sam-

ples like Cu-TTP in our experiments. As mentioned above, since diaminotriazine can act as a “proton pump”, H<sup>+</sup> will transfer quickly to \*CO to generate the \*CHO thus preventing the departure of \*CO to form CO, leading to the high selectivity of CH<sub>4</sub>. Based on the experiment results and theoretical calculations, we propose a possible CO<sub>2</sub>RR pathway from CO<sub>2</sub> to CH<sub>4</sub> on Cu-TDPP-NS. During the CO<sub>2</sub>RR process, CO<sub>2</sub> is firstly adsorbed and activated on the Cu center, which are quickly transformed into \*COOH. The intermediate \*COOH can form hydrogen bond with the amino group of Cu-TDPP-NS. Subsequently, \*CO intermediate is generated. Meanwhile, diaminotriazine acting as the “proton pump”, can facilitate the quick transfer of H<sup>+</sup> to combine with \*CO to generate \*CHO, thus preventing the departure of \*CO to form CO and leading to outstanding selectivity of CH<sub>4</sub>. Then the \*HCOH, \*CH, \*CH<sub>2</sub> and \*CH<sub>3</sub> intermediates generate in turn coupling with the multi-step proton-electron transfer processes. Finally, the produced CH<sub>4</sub> is quickly desorbed from catalyst surface and efficiently transferred into electrolyte to finish the catalysis process.

## Conclusion

In summary, we have synthesized a kind of Cu-porphyrin-based large-scale ( $\approx 1.5$   $\mu\text{m}$ ) and ultrathin ( $\approx 5$  nm) nano-sheet and explored its CO<sub>2</sub>RR performance in neutral media. Specifically, Cu-TDPP-NS exhibits a superior FE<sub>CH<sub>4</sub></sub> of 70% with high current density ( $-183.0$  mA cm<sup>-2</sup>) at  $-1.6$  V under neutral condition and maintains FE<sub>CH<sub>4</sub></sub> > 51% over a wide potential range ( $-1.5$  to  $-1.7$  V). The electrochemical CO<sub>2</sub>RR under neutral conditions has been rarely reported and, to our knowledge, the achieved performance is even superior to that of most CO<sub>2</sub>RR systems under alkaline condition. Based on our experimental results and DFT calculations, the high performance may be attributed to the construction of numerous hydrogen-bonding networks through the integration of diaminotriazine with Cu-porphyrin, which is greatly beneficial for intermediate stabilization and proton migration. Besides, the stability of Cu-TDPP-NS after electrocatalytic CO<sub>2</sub>RR process has been proved by sufficient characterizations like XAS, XPS, HR-TEM and elemental mapping tests. This strategy opens great perspectives for the design of novel hydrogen-bonding-based materials for efficient CO<sub>2</sub>RR in production of hydrocarbons and might contribute to the exploration of powerful protocols to address CO<sub>2</sub> problems.

## Acknowledgements

This work was financially supported by NSFC (No. 21871141, 21871142, 22071109 and 21901122); the NSF of Jiangsu Province of China (No. BK20171032); the Natural Science Research of Jiangsu Higher Education Institutions of China (No. 19KJB150011) and Project funded by China Postdoctoral Science Foundation (No. 2019M651873); Priority Academic Program Development of Jiangsu Higher Education

Institutions; and the Foundation of Jiangsu Collaborative Innovation Center of Biomedical Functional Materials.

### Conflict of Interest

The authors declare no conflict of interest.

**Keywords:** electroreduction · hydrogen bonds · methane · nanosheets

- [1] a) M. He, Y. Sun, B. Han, *Angew. Chem. Int. Ed.* **2013**, *52*, 9620–9633; *Angew. Chem.* **2013**, *125*, 9798–9812; b) S. Liu, X. F. Lu, J. Xiao, X. Wang, X. W. Lou, *Angew. Chem. Int. Ed.* **2019**, *58*, 13828–13833; *Angew. Chem.* **2019**, *131*, 13966–13971.
- [2] a) Y.-R. Wang, Q. Huang, C.-T. He, Y. Chen, J. Liu, F.-C. Shen, Y.-Q. Lan, *Nat. Commun.* **2018**, *9*, 4466; b) Y.-R. Wang, R.-X. Yang, Y. Chen, G.-K. Gao, Y.-J. Wang, S.-L. Li, Y.-Q. Lan, *Sci. Bull.* **2020**, *65*, 1635–1642.
- [3] a) L. Han, S. Song, M. Liu, S. Yao, Z. Liang, H. Cheng, Z. Ren, W. Liu, R. Lin, G. Qi, X. Liu, Q. Wu, J. Luo, H. L. Xin, *J. Am. Chem. Soc.* **2020**, *142*, 12563–12567; b) Q. Hu, Z. Han, X. Wang, G. Li, Z. Wang, X. Huang, H. Yang, X. Ren, Q. Zhang, J. Liu, C. He, *Angew. Chem. Int. Ed.* **2020**, *59*, 19054–19059; *Angew. Chem.* **2020**, *132*, 19216–19221.
- [4] a) P. De Luna, C. Hahn, D. Higgins, S. A. Jaffer, T. F. Jaramillo, E. H. Sargent, *Science* **2019**, *364*, eaav3506; b) D. Gao, R. M. Arán-Ais, H. S. Jeon, B. Roldan Cuenya, *Nat. Catal.* **2019**, *2*, 198–210; c) A. Wagner, C. D. Sahm, E. Reisner, *Nat. Catal.* **2020**, *3*, 775–786.
- [5] a) W. Ma, S. Xie, T. Liu, Q. Fan, J. Ye, F. Sun, Z. Jiang, Q. Zhang, J. Cheng, Y. Wang, *Nat. Catal.* **2020**, *3*, 478–487; b) S. Nitopi, E. Bertheussen, S. B. Scott, X. Liu, A. K. Engstfeld, S. Horch, B. Seger, I. E. L. Stephens, K. Chan, C. Hahn, J. K. Nørskov, T. F. Jaramillo, I. Chorkendorff, *Chem. Rev.* **2019**, *119*, 7610–7672.
- [6] a) Z. Gu, H. Shen, L. Shang, X. Lv, L. Qian, G. Zheng, *Small Methods* **2018**, *2*, 1800121; b) Y. Y. Birdja, E. Pérez-Gallent, M. C. Figueiredo, A. J. Göttele, F. Calle-Vallejo, M. T. M. Koper, *Nat. Energy* **2019**, *4*, 732–745.
- [7] a) C. Yang, S. Li, Z. Zhang, H. Wang, H. Liu, F. Jiao, Z. Guo, X. Zhang, W. Hu, *Small* **2020**, *16*, 2001847; b) S. Liu, H. Yang, X. Huang, L. Liu, W. Cai, J. Gao, X. Li, T. Zhang, Y. Huang, B. Liu, *Adv. Funct. Mater.* **2018**, *28*, 1800499.
- [8] a) W. Ju, A. Bagger, X. Wang, Y. Tsai, F. Luo, T. Möller, H. Wang, J. Rossmeisl, A. S. Varela, P. Strasser, *ACS Energy Lett.* **2019**, *4*, 1663–1671; b) Y. Zheng, A. Vasileff, X. Zhou, Y. Jiao, M. Jaroniec, S.-Z. Qiao, *J. Am. Chem. Soc.* **2019**, *141*, 7646–7659.
- [9] L. Wang, W. Chen, D. Zhang, Y. Du, R. Amal, S. Qiao, J. Wu, Z. Yin, *Chem. Soc. Rev.* **2019**, *48*, 5310–5349.
- [10] a) Y. J. Sa, C. W. Lee, S. Y. Lee, J. Na, U. Lee, Y. J. Hwang, *Chem. Soc. Rev.* **2020**, *49*, 6632–6665; b) Q. Zhang, J. Guan, *Adv. Funct. Mater.* **2020**, *30*, 2000768.
- [11] a) R. Cao, J.-D. Yi, R. Xie, Z.-L. Xie, G.-L. Chai, T.-F. Liu, R.-P. Chen, Y.-B. Huang, *Angew. Chem. Int. Ed.* **2020**, *59*, 23641–23648; *Angew. Chem.* **2020**, *132*, 23849–23856; b) P. Gotico, L. Roupnel, R. Guillot, M. Sircoglou, W. Leibl, Z. Halime, A. Aukauloo, *Angew. Chem. Int. Ed.* **2020**, *59*, 22451–22455; *Angew. Chem.* **2020**, *132*, 22637–22641.
- [12] a) B. Wang, R.-B. Lin, Z. Zhang, S. Xiang, B. Chen, *J. Am. Chem. Soc.* **2020**, *142*, 14399–14416; b) M. A. Little, A. I. Cooper, *Adv. Funct. Mater.* **2020**, *30*, 1909842; c) I. Hisaki, C. Xin, K. Takahashi, T. Nakamura, *Angew. Chem. Int. Ed.* **2019**, *58*, 11160–11170; *Angew. Chem.* **2019**, *131*, 11278–11288; d) P. Li, Z. Chen, M. R. Ryder, C. L. Stern, Q.-H. Guo, X. Wang, O. K. Farha, J. F. Stoddart, *J. Am. Chem. Soc.* **2019**, *141*, 12998–13002.
- [13] a) K.-i. Otake, K. Otsubo, T. Komatsu, S. Dekura, J. M. Taylor, R. Ikeda, K. Sugimoto, A. Fujiwara, C.-P. Chou, A. W. Sakti, Y. Nishimura, H. Nakai, H. Kitagawa, *Nat. Commun.* **2020**, *11*, 843; b) X.-M. Li, L.-Z. Dong, J. Liu, W.-X. Ji, S.-L. Li, Y.-Q. Lan, *Chem* **2020**, *6*, 2272–2282.
- [14] Z. Weng, Y. Wu, M. Wang, J. Jiang, K. Yang, S. Huo, X.-F. Wang, Q. Ma, G. W. Brudvig, V. S. Batista, Y. Liang, Z. Feng, H. Wang, *Nat. Commun.* **2018**, *9*, 415.
- [15] W. Yang, B. Li, H. Wang, O. Alduhaish, K. Alfooty, M. A. Zayed, P. Li, H. D. Arman, B. Chen, *Cryst. Growth Des.* **2015**, *15*, 2000–2004.
- [16] Y. Zhao, J. Wang, R. Pei, *J. Am. Chem. Soc.* **2020**, *142*, 10331–10336.
- [17] a) Y. Wang, Z. Chen, P. Han, Y. Du, Z. Gu, X. Xu, G. Zheng, *ACS Catal.* **2018**, *8*, 7113–7119; b) P. Grosse, D. Gao, F. Scholten, I. Sinev, H. Mistry, B. Roldán Cuenya, *Angew. Chem. Int. Ed.* **2018**, *57*, 6192–6197; *Angew. Chem.* **2018**, *130*, 6300–6305; c) H. Pan, C. J. Barile, *Energy Environ. Sci.* **2020**, *13*, 3567–3578.
- [18] a) H. Zhong, M. Ghorbani-Asl, K. H. Ly, J. Zhang, J. Ge, M. Wang, Z. Liao, D. Makarov, E. Zschech, E. Brunner, I. M. Weidinger, J. Zhang, A. V. Krasheninnikov, S. Kaskel, R. Dong, X. Feng, *Nat. Commun.* **2020**, *11*, 1409; b) X.-F. Qiu, H.-L. Zhu, J.-R. Huang, P.-Q. Liao, X.-M. Chen, *J. Am. Chem. Soc.* **2021**, *143*, 7242–7246; c) J. Liu, D. Yang, Y. Zhou, G. Zhang, G. Xing, Y. Liu, Y. Ma, O. Terasaki, S. Yang, L. Chen, *Angew. Chem. Int. Ed.* **2021**, *60*, 14473–14479; *Angew. Chem.* **2021**, *133*, 14594–14600.
- [19] Y. Liu, C. C. L. McCrory, *Nat. Commun.* **2019**, *10*, 1683.
- [20] R. Subbaraman, D. Tripkovic, D. Strmcnik, K.-C. Chang, M. Uchimura, A. P. Paulikas, V. Stamenkovic, N. M. Markovic, *Science* **2011**, *334*, 1256.

Manuscript received: June 23, 2021

Accepted manuscript online: August 12, 2021

Version of record online: August 26, 2021